Climate Dynamics (1997) 13:703–716

Climate Dynamics

Errors in estimating spherical harmonic coefficients from partially sampled GCM output

F. W. Zwiers[1,*], S. S. Shen[2]

[1] Canadian Centre for Climate Modelling and Analysis, Atmospheric Environment Service, PO Box 1700, Victoria, Canada V8W 2Y2
[2] Department of Mathematical Sciences, University of Alberta, Edmonton, Canada T6G 2G1

Received: 19 April 1996 / Accepted: 10 April 1997

Abstract. This study describes a method of calculating the mean squared error (MSE) incurred when estimating the spherical harmonic coefficients of a climatological field that is sampled at a small network of points. The method can also be applied to the coefficients of any other set of orthonormal basis functions that are defined on the sphere. It, therefore, provides a formalism that can be applied in a variety of contexts, such as in climate change detection, where inferences are attempted about fingerprint coefficients that are imperfectly estimated from observational data. By incorporating the fingerprint as part of a set of basis functions, the methodology can be used to estimate the sampling error in the fingerprint coefficient. The MSE is expressed in terms of the spherical harmonics (or other orthonormal expansion) of the empirical orthogonal functions (EOFs), the locations of the points in the network and a set of weights that are applied at these points. The weights are optimised by minimising the expected MSE. The method is applied to a number of network configurations using monthly-mean screen temperature and 500 mb height simulated by the Canadian Climate Centre 2nd generation general circulation model in an ensemble of six 10-year simulations. In comparison with uniform weighting, optimal weighting can reduce the MSE by an order of magnitude or more for some spherical harmonic coefficients and some network configurations. Also, the MSEs vary seasonally for each network. In particular, the relative MSE of low order spherical harmonic coefficients is found to be larger in DJF than in JJA. We demonstrate how MSEs improve with increasing network density and identify graphically, the coefficients that can be estimated reliably with each network configuration.

1 Introduction

The errors incurred by using the data from a limited number of observation stations to estimate a climate-index, such as the globally averaged annual mean temperature, have been an important concern for climatologists in recent years, particularly in the context of climate change detection, where a great deal of attention has been paid to the temporal variations of globally and hemispherically averaged temperature. We therefore have two objectives. The first is to provide a method to evaluate the minimal mean squared sampling errors (MSEs) incurred in estimating the spherical harmonic coefficients of a climatological field from observations taken at a network with a small number of stations. The method is easily adapted to the problem of evaluating the sampling error of the estimated time varying coefficients of an arbitrary function on the sphere (such as a climate change "fingerprint"; Barnett and Schlesinger 1987; Barnett et al. 1991; Hasselmann 1993; North et al. 1995), provided the function can be incorporated into a complete basis for the square integrable functions on the sphere. The second objective is to illustrate the methodology by applying it to output of the Canadian Climate Centre 2nd generation general circulation model (CCC GCM2; McFarlane et al. 1992; Boer et al. 1992) sampled by a number of observing networks. We show that the low-order spherical harmonic coefficients can be reasonably well estimated from a small network of judiciously located stations. We will also show that the MSE varies seasonally in accordance with seasonal changes in the variance/covariance structure of the climatological fields we consider.

Our approach of optimally weighting the observations to minimise the MSE is similar to that often used in objective analysis (Gandin 1963; Thiebaux 1976; Thiebaux and Pedder 1987; Daley 1991; Vinnikov et al. 1990; Reynolds and Smith 1994; Smith et al. 1994). It differs from objective analysis in the way in which the spatial covariance function of the field is represented. Rather than using simple models that characterise the covariance between locations as a function of separation, we use the full covariance structure of the field as represented by its empirical orthogonal functions (EOFs; the eigen-functions of the associated covariance kernel).

Previous work by one of us has been concerned with computing the MSEs using spatial covariance structure estimates derived from observations (Shen et al. 1994) and

* Also affiliated with the Department of Mathematics and Statistics, University of Victoria, Victoria, BC, Canada, V8W 2Y2

from a simple linear energy balance model (Shen et al. 1996). In the latter paper it is shown that the climate simulated by a linear white-noise-forced energy-balance model with constant coefficients has a spatial covariance structure that is homogeneous on the sphere and therefore has spherical harmonics as its eigen-functions. Climate models that are more complex than this, and observations, have covariance structures that are not homogeneous in space and are thus difficult to characterise analytically. It then becomes important to have available sufficiently large samples that can be used to construct accurate estimates of the spatial covariance structure and the associated eigen-functions.

The present study is distinct from that of Shen et al. (1994) in several respects. Shen et al. use the Jones et al. (1986a, b) screen-temperature data set. In contrast, we use CCC GCM2 simulated screen temperature and 500 mb height to examine sampling errors in monthly mean spherical harmonic coefficients. We also examine how the errors vary with the annual cycle. We use a cross-validation technique to insure that our MSE estimates remain robust when the optimal weights are used with independent data from the same GCM. We show that unvalidated MSE estimates are optimistically biased when small samples are used to estimate the field's spatial covariance structure. Finally, our method for estimating the EOFs is different from that used by Shen et al. (1994).

The plan for the remainder of this study is as follows: the equation for the MSE is derived in Sect. 2. The climate model and its output are briefly described in Sect. 3. In Section 4, we describe the computation of the EOFs of the simulated climate data and the eigen-spectra of monthly mean 500 mb height (Z_{500}) and the screen temperature (T_s). In Sect. 5 we describe the computation of the optimal weights for estimating spherical harmonic coefficients when observations are taken from small networks. In comparison with equal weighting of all network locations, optimal weighting significantly reduces the expected sampling error. Section 6 contains a summary and conclusions.

2 The MSE equation

Meteorological fields are regarded as lying on a perfect sphere with unit radius. The unit outward normal vector $\vec{\mathbf{n}} = (\cos\phi\cos\theta, \cos\phi\sin\theta, \sin\phi)$, where ϕ and θ are longitude and latitude respectively, gives the position on the sphere. A nonuniform time varying anomaly field $S(\vec{\mathbf{n}}, t)$, where S is either monthly mean T_s or Z_{500}, and where anomalies are taken relative to the annual cycle, can be expanded in spherical harmonics Y_{lm} as

$$S(\vec{\mathbf{n}}, t) = \sum_{l=0}^{\infty} \sum_{m=-l}^{l} S_{lm}(t)\, Y_{lm}(\vec{\mathbf{n}}). \tag{1}$$

The spherical harmonic coefficient $S_{lm}(t)$ is determined by

$$S_{lm}(t) = \int_{4\pi} d\vec{\mathbf{n}}\, S(\vec{\mathbf{n}}, t)\; Y^*_{lm}(\vec{\mathbf{n}}), \tag{2}$$

where * denotes complex conjugate. Our objective is to calculate the mean squared error incurred in estimating $S_{lm}(t)$ from observations taken at a small number of points on the sphere.

Suppose we sample the anomaly field at N points $(\vec{\mathbf{n}}_1, \vec{\mathbf{n}}_2, \cdots, \vec{\mathbf{n}}_N)$. To estimate $S_{lm}(t)$ we approximate Eq. (2) as a Riemann sum

$$\hat{S}_{lm}(t) = \sum_{j=1}^{N} S(\vec{\mathbf{n}}_j, t)\; Y^*_{lm}(\vec{\mathbf{n}}_j)\; w_j^{(lm)} \tag{3}$$

in which $w_j^{(lm)}$ is the area of a region on the surface of the unit sphere around the point $\vec{\mathbf{n}}_j$. These areas, which we will simply refer to as weights $w_j^{(lm)}$, are of course constrained by

$$\sum_{j=1}^{N} w_j^{(lm)} = 4\pi. \tag{4}$$

Our problem then is to select a set of optimal weights so that the estimated $\hat{S}_{lm}(t)$ will be as close as possible to the exact $S_{lm}(t)$ on average. That is, we wish to find the weights that minimise the mean squared error

$$\varepsilon^2_{(lm)} = \langle |S_{lm}(t) - \hat{S}_{lm}(t)|^2 \rangle, \tag{5}$$

where $\langle\cdot\rangle$ denotes ensemble average (i.e., the expectation operator). We assume, for now, that the monthly means of S are the output of a 2nd order stationary stochastic process so that the covariance structure of S is the same at all times of the year. We also assume that the process is ergodic to ensure that the covariance structure is estimable. Later we will relax the temporal stationarity assumption. In addition, we make the regularity assumption that each realisation of S is square integrable on the sphere so that it can be represented as an expansion in spherical harmonics.

The MSE Eq. (5) can be re-expressed as

$$\begin{aligned}\varepsilon^2_{(lm)} &= \langle |S_{(lm)}(t)|^2 \rangle - 2\,\Re(\langle S_{(lm)(t)} \hat{S}_{(lm)}(t) \rangle) + \langle |\hat{S}_{(lm)}(t)|^2 \rangle \\ &= \int d\vec{\mathbf{n}} \int d\vec{\mathbf{n}}'\; \rho(\vec{\mathbf{n}}, \vec{\mathbf{n}}')\, Y^*_{lm}(\vec{\mathbf{n}})\, Y_{lm}(\vec{\mathbf{n}}') \\ &\quad - 2\,\Re\left(\sum_{i=1}^{N} w_i^{(lm)} \int d\vec{\mathbf{n}}\, \rho(\vec{\mathbf{n}}, \vec{\mathbf{n}}_i)\, Y^*_{lm}(\vec{\mathbf{n}})\; Y_{lm}(\vec{\mathbf{n}}_i) \right) \\ &\quad + \sum_{i,j=1}^{N} w_i^{(lm)} w_j^{(lm)}\; \rho(\vec{\mathbf{n}}_i, \vec{\mathbf{n}}_j)\, Y^*_{lm}(\vec{\mathbf{n}}_i)\, Y_{lm}(\vec{\mathbf{n}}_j)\end{aligned} \tag{6}$$

where $\Re(\cdot)$ denotes the real part of $(\cdot)$ and

$$\rho(\vec{\mathbf{n}}, \vec{\mathbf{n}}') = \langle S(\vec{\mathbf{n}}, t)\; S(\vec{\mathbf{n}}', t) \rangle \tag{7}$$

is the spatial covariance. This covariance may be viewed as the kernel of an integral operator on the unit sphere, whose eigen-functions $\psi_k(\vec{\mathbf{n}})$ (called EOFs or eigen-modes) and eigen-values λ_k (the variances of the corresponding eigen-function coefficients) are defined by

$$\int d\vec{\mathbf{n}}'\; \rho(\vec{\mathbf{n}}, \vec{\mathbf{n}}')\psi_k(\vec{\mathbf{n}}') = \lambda_k\; \psi_k(\vec{\mathbf{n}}), \quad (k = 1, 2, 3, \cdots). \tag{8}$$

Our regularity assumption ensures that the EOFs are orthogonal so that they form a complete basis for the square integrable functions defined on the unit sphere just as is the case for the spherical harmonics. The EOFs are also the principal axes of the covariance kernel. That is,

$$\rho(\vec{\mathbf{n}}, \vec{\mathbf{n}}') = \sum_{k=1}^{\infty} \lambda_k \psi_k(\vec{\mathbf{n}}) \psi_k(\vec{\mathbf{n}}'). \tag{9}$$

Using this fact, one can then easily demonstrate that the anomaly field S can be expanded in the eigen-functions as

$$S(\vec{\mathbf{n}}, t) = \sum_{k=1}^{\infty} S_k(t)\psi_k(\vec{\mathbf{n}}), \tag{10}$$

where

$$S_k(t) = \int d\vec{\mathbf{n}}\; S(\vec{\mathbf{n}}, t)\psi_k(\vec{\mathbf{n}}). \tag{11}$$

These coefficients, often referred to as principal components, are uncorrelated and have variance

$$\langle |S_k(t)|^2 \rangle = \lambda_k. \tag{12}$$

The EOFs can be represented by a spherical harmonic function expansion

$$\psi_k(\vec{\mathbf{n}}) = \sum_{l=0}^{\infty} \sum_{m=-l}^{l} \psi_{k,lm} Y_{lm}(\vec{\mathbf{n}}) \tag{13}$$

where

$$\psi_{k,lm} = \int d\vec{\mathbf{n}}\; \psi_k(\vec{\mathbf{n}}) Y^*_{lm}(\vec{\mathbf{n}}). \tag{14}$$

Using this representation, expression (6) for the MSE can be re-written as (Shen et al. 1994; Kim et al. 1996)

$$\varepsilon^2_{(lm)} = \sum_{k=1}^{\infty} \lambda_k |\psi_{k,lm} - \sum_{i=1}^{N} w_i^{(lm)} \psi_k(\vec{\mathbf{n}}_i) Y^*_{lm}(\vec{\mathbf{n}}_i)|^2. \tag{15}$$

The summation with respect to the station number i is simply a numerical approximation to the integral (14). Hence, the sampling error for a given spherical harmonic coefficient is the accumulation of the numerical integration errors for all the successive EOFs weighted by the corresponding eigen-values.

3 CCC GCM2

CCC GCM2 is a spectral model with T32 horizontal resolution and 10 levels in the vertical. The model and its climate are described by McFarlane et al. (1992). CCC GCM2 can be run in a variety of configurations. These include an atmosphere only mode, in which the sea-surface temperature (SST) and sea–ice extent are prescribed to follow either the climatological annual cycle or time varying observations, and coupled modes in which the model is run with either a mixed layer or a dynamical ocean model. A thermodynamic ice model is used in both coupled modes.

The data used in this study were obtained from an ensemble of six 10-year AMIP simulations (see Gates 1992, for a description of AMIP, the Atmospheric Model Intercomparison Project). Each simulation is started from different initial conditions and is forced with the observed evolution of the SST and sea–ice extent between January, 1979 and December, 1988. Zwiers (1996) describes the CCC GCM2 AMIP experiment in detail. Five months of data were discarded from the beginning of each simulation to allow equilibration of the land surface processes. The last month was also not used. We therefore had available 114 monthly means of T_s and Z_{500} from each of the six simulations (i.e., a total of 684 monthly means).

The data were processed in three steps prior to analysis. First, to keep the eigen-analysis to a manageable size, we smoothed the data spatially by truncating it to T21 spectral resolution. That is, the time dependent spherical harmonic coefficients $S_{lm}(t)$ for $l > 21$ were set to zero. For both T_s and Z_{500}, the unresolved scales contain very little variance and therefore do not substantially affect our results. Secondly, we removed the 114 month means from each simulation to remove the effects of minor differences in the way in which the simulations were performed (Zwiers 1996). Finally, the annual cycle common to the six 114 month time series was removed by fitting the main Fourier component and its first three harmonics to the ensemble mean time series.

We now briefly discuss some aspects of the spatial covariance structure simulated by CCC GCM2 and show that this structure is both inhomogeneous and anisotropic. It is therefore necessary to use EOFs to fully account for the details of this complex covariance structure when deriving optimal weights to minimise the MSE (Eq. (6)) of spherical harmonic (or other basis function) coefficient estimates.

Figures 1 and 2 display the standard deviations of monthly mean T_s and Z_{500} respectively in DJF. Figure 1 can be compared with Shea (1986) who displays the interannual variance of January mean T_s (see Shea's Figs. TMP-09) as computed from station data. The structure and magnitude of the screen temperature variability

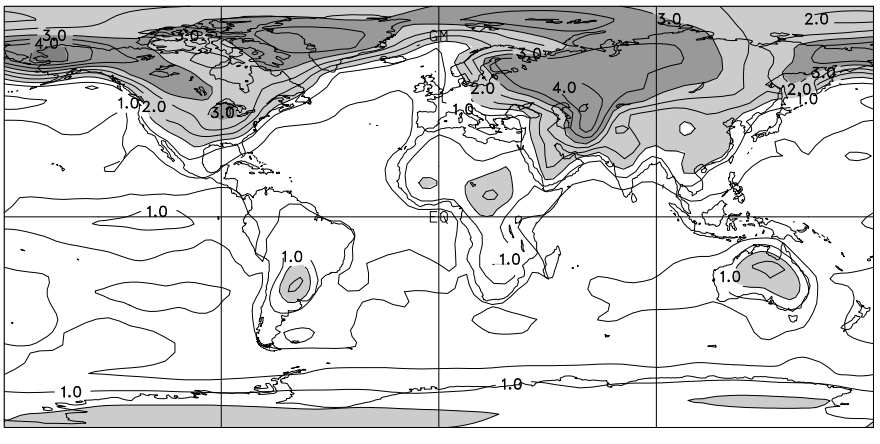

Fig. 1. Standard deviation of CCC GCM2 monthly mean screen temperature in DJF. Contour interval: 0.5 °C. Standard deviations greater than 1 °C are *shaded*

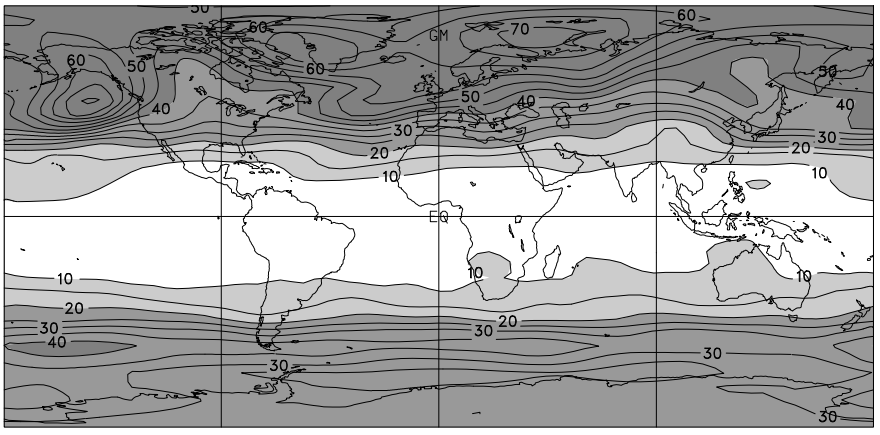

Fig. 2. Standard deviation of CCC GCM2 monthly mean 500 hPa height in DJF. Contour interval: 5 *m*. Standard deviations greater than 10 *m* are *shaded*

simulated by CCC GCM2 compares very well with that which is observed. Figure 2 can be compared with Oort (1983) who displays a comparable diagram computed from 1958–73 NMC analyses (see Oort's Fig. A26). Z_{500} variations simulated by CCC GCM2 are somewhat weaker than are observed (see also Zwiers 1996) but their structure is highly realistic.

Figure 3 displays teleconnection maps for monthly mean Z_{500} simulated in DJF for reference points fixed at (47 °N, 90 °W) and (2 °N, 180 °W). Figure 3a shows an asymmetrical wave train in the zonal direction with a decorrelation length of about 2,500 km. Weak anti-correlated nodes can be seen to the northeast and southeast of the reference point. Behaviour in the Southern Hemisphere mid-latitudes (not shown) is similar. Figure 3b shows that DJF monthly mean 500 mb heights are very strongly correlated every where in the tropics. Zwiers (1996) shows that most of this coherent variation is driven by variations in tropical SST. We also see evidence of the model's extra-tropical dynamical response to SST variation in the form of the PNA pattern (Wallace and Gutzler 1981) that can be seen over the northeastern Pacific

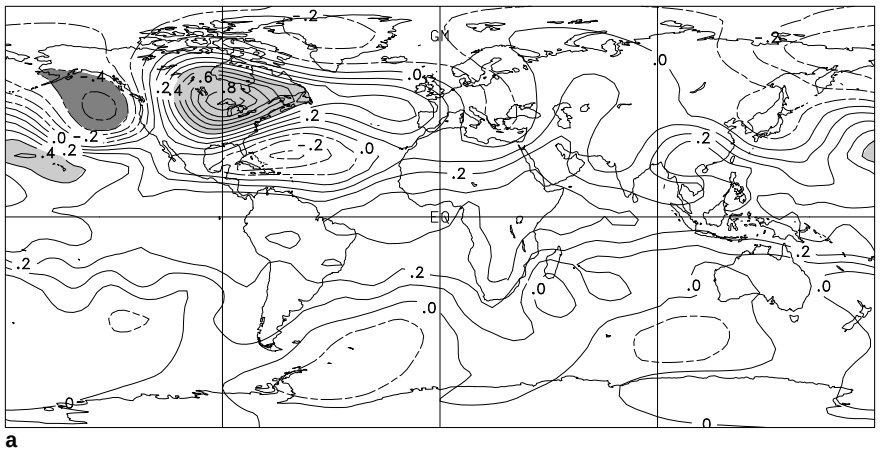

a

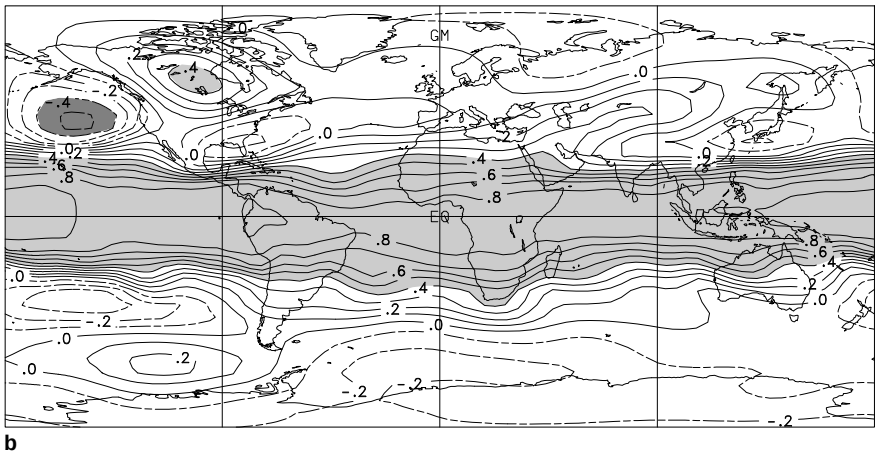

b

Fig. 3a,b. The correlation in DJF between CCC GCM2 monthly mean Z_{500} at a fixed point and all other locations on the globe: **a** 47 °N, 90 °W, and **b** 2 °N, 180 °W. Contour interval: 0.1. Correlations with magnitude greater than 0.4 are *shaded*

and North America. The JJA teleconnection patterns (not shown) are similar, except that the PNA is not evident in patterns centred on tropical locations.

4 The EOFs

Since the GCM output is represented with spherical harmonic expansions it is advantageous to compute the EOFs in the spectral domain as well. Therefore, instead of discretising the eigen-value problem for the linear integral operator in physical space (see Eq. (8)) we re-express the operator in the spectral domain. Since the data are truncated at T21 resolution, the equivalent matrix/vector eigen-problem is

$$\sum_{l'=0}^{L}\sum_{m'=-l'}^{l'} \langle S_{lm} S_{l'm'}\rangle \psi^*_{k,l'm'} = \lambda_k \psi_{k,lm} \quad (k = 1, 2, 3, \cdots), \tag{16}$$

where $L = 21$.

In the GCM a fast numerical quadrature scheme is used to transform back and forth between spectral and physical space. This operator is a linear transformation acting on the field at the model's grid points. Hence there is a natural discretisation of Eq. (8) that solves the same eigen-analysis problem in physical space as Eq. (16).

It is computationally advantageous to solve a global or hemispheric eigen-problem in the spectral domain rather than the physical domain because it is more compactly represented and because area weighting of the model's grid points is implicitly taken into account. The spectral form of the problem is solved using conventional software by re-expressing Eq. (16) in real matrix-vector form as

$$\mathscr{R}_S \vec{\psi}_{S_k} = \lambda_k \vec{\psi}_{S_k} \tag{17}$$

where $\mathscr{R}_S$ is the $(L+1)^2 \times (L+1)^2$ covariance matrix of the real and imaginary components of the spectral coefficients of the spectrally truncated anomaly field S, and $\vec{\psi}_{S_k}$ is the corresponding $(L+1)^2$ dimensional vector that contains the real and imaginary spherical harmonic coefficients of the kth eigen-function. When using T21 truncation the eigen-analysis takes place in a $(21+1)^2 = 484$ dimensional vector space. In contrast, the Gaussian grid that corresponds to the T21 truncation carries the same information but has $64 \times 32 = 2048$ points.

In either case the number of non-zero eigen-values is limited by the number of non-zero real and imaginary spherical harmonic coefficients. In the spectral domain the monthly means are realised in an $(L+1)^2$ dimensional vector space. Since the transformation to physical space is linear and one-to-one, the discretised realisations in physical space are restricted to an $(L+1)^2$ dimensional subspace of the P dimensional physical space.

To solve Eq. (17) we must estimate $\mathscr{R}_S$. To do this let $\vec{S}_S$ represent the $(L+1)^2$ dimensional vector that contains the real and imaginary spherical harmonic coefficients of the spectrally truncated anomaly field S and let $\vec{S}_{S_q}$, $q = 1, \ldots, Q$ be a collection of Q realisations of $\vec{S}_S$. Construct an $(L+1)^2 \times Q$ data matrix $\mathscr{S}$ that has $\vec{S}_{S_q}$ as its qth column. Because $\vec{S}_S$ represents an anomaly field (i.e., the annual cycle has been removed) it is not necessary to remove the mean from the realizations of $\vec{S}_S$. Hence $\mathscr{R}_S$ can simply be estimated as

$$\hat{\mathscr{R}}_S = \frac{1}{Q}\sum_{q=1}^{Q} \vec{S}_{S_q}\vec{S}'_{S_q} = \frac{1}{Q}\mathscr{S}\mathscr{S}' \tag{18}$$

Note that the number of non zero eigen-values obtained when solving Eq. (17) with $\hat{\mathscr{R}}_S$ will be the dimension of the column space of $\hat{\mathscr{R}}_S$ which is $min\{Q, (L+1)^2\}$.

We use Eqs. (17) and (18) to estimate the EOFs of monthly mean T_s and Z_{500} simulated by CCC GCM2 in DJF, JJA and for all months of the year combined. We assume that the climate is roughly stationary during the solstice seasons and therefore that the EOFs obtained from the DJF and JJA samples of monthly means are representative of the monthly mean spatial covariance structure during those seasons. The DJF and JJA parts of the model output data set contain $Q = 162$ and $Q = 180$ monthly mean fields respectively. We can not make the stationarity assumption for the EOFs computed from the full data set which contains $Q = 684$ monthly mean fields. However, the EOFs computed from the full data set can be interpreted as the modes that capture the model's variation on the 2-month to 10-year time scale as in Kim and North (1993).

The eigen-spectra obtained from our eigen-analyses are briefly summarised in the Table 1. As others have found, the magnitudes of the eigen-values decrease almost exponentially with increasing mode number (not shown). Table 1 shows that the eigen-spectrum of both T_s and Z_{500} is slightly flatter in JJA than in DJF. In the case of T_s greater instability over the NH land surface during summer probably creates relatively more small-scale variability in NH summer. Similarly, it is likely that more Z_{500} variability originates from relatively small-scale thermal sources in JJA than in DJF. Table 1 also shows that the eigen-spectrum of T_s is substantially flatter than that of Z_{500} reflecting the fact that T_s variations occur on a greater range of spatial scales than Z_{500} variations. Finally, we see that for both variables a much wider eigen-spectrum is needed to capture the total variance structure aggregated over all months of the year. The reason is that for both fields, the low-order solstice season eigen-modes are confined entirely to the winter hemisphere. A larger set of EOFs containing both types of modes is required to capture the strong variations that occur in both hemispheres in the full data set.

Figure 4 displays the first four DJF T_s EOFs. All four modes (12.6%, 10.2%, 7.3% and 5.7% of variance) primarily describe variations over NH land masses and ice covered areas. Similarly, the first four modes in JJA (18.6%, 8.2%, 6.8% and 6.0% of variance, not shown)

Table 1. The percentage of variances explained by the first ten modes and, in parentheses, the number of nodes required to explain 90% of the simulated variance

Variable	DJF	JJA	All months
Screen Temperature	57.1 (46)	56.2 (50)	42.5 (84)
500 hPa height	62.4 (30)	57.8 (37)	51.8 (43)

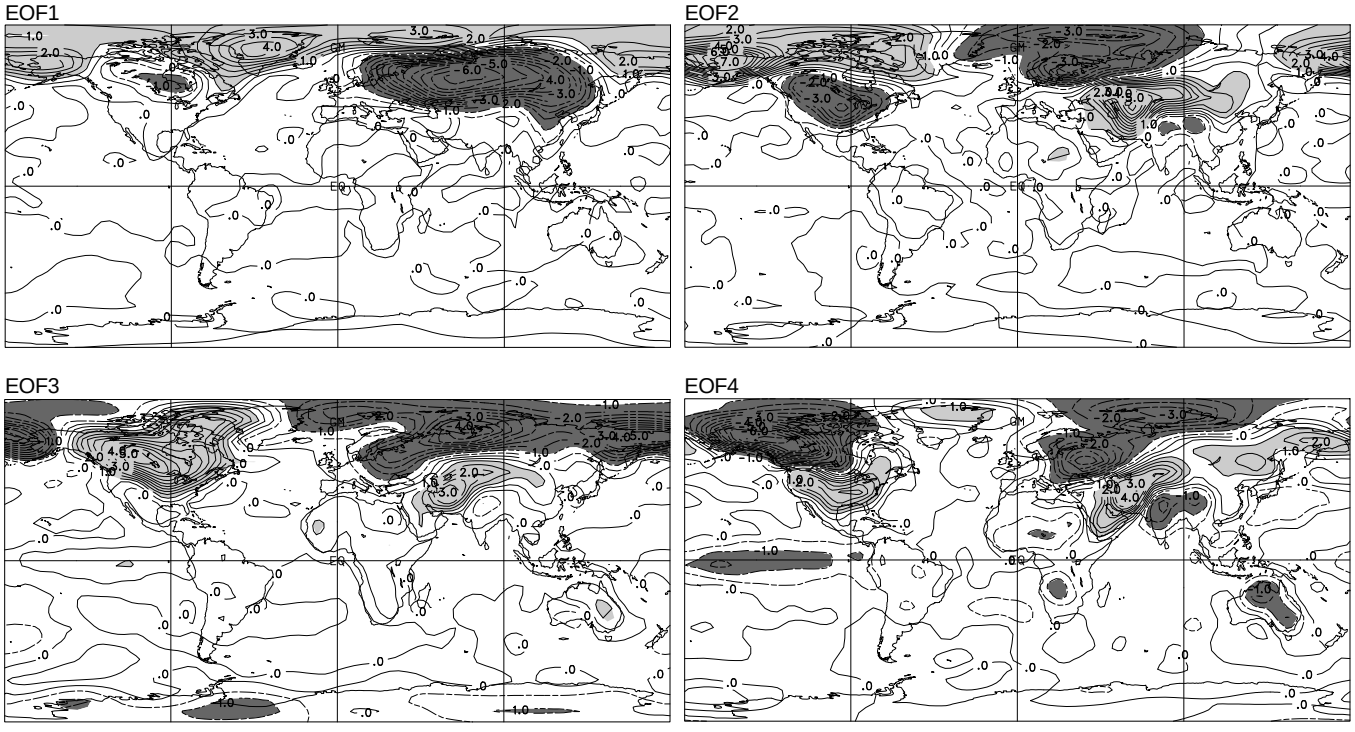

Fig. 4. EOFs 1–4 of CCC GCM2 monthly mean DJF T_s explaining 12.6%, 10.2%, 7.3% and 5.7% of variance respectively

appear to describe, primarily, screen temperature variations at high southern latitudes.

Note that there is generally less information in these patterns than the size of the data set from which they are computed would perhaps suggest. CCC GCM2 screen temperature is strongly influenced over the oceans by the prescribed SSTs. Since these prescriptions evolve identically in each simulation, there is a substantial overlap in information content between simulations.

Figure 5 displays the NH part of the first four DJF Z_{500} EOFs. EOF 1 strongly resembles the North Atlantic Oscillation pattern (Barnston and Livezey 1987) except that the centre of action over Greenland is slightly exaggerated and the entire pattern is rotated slightly eastward. This mode explains 13.8% of variance in the model while in Barnston and Livezey's (1987) analysis of NMC 700 hPa height analyses it explains 11.1% of variance. EOF 2, which explains 9.4% of variance, resembles the Western Atlantic Pattern documented by Wallace and Gutzler (1981). EOF 3 (8.9% of variance) is a somewhat contorted PNA pattern (Wallace and Gutzler 1981; Barnston and Livezey 1987) that is shifted slightly eastward, has an exaggerated Aleutian low, and a "centre of action" over the southeastern USA that is too weak. In Barnston and Livezey's (1987) analysis, the PNA explains somewhat more variance (10.8%) than it does in the simulated climate. EOF 4 (6.5% of variance) appears to be a mixture of the PNA pattern and the Eastern Atlantic pattern of Wallace and Gutzler (1981).

The apparent mixing of modes appears to be a problem with EOF analysis performed in the spectral domain. In the physical domain one is able to achieve patterns with "simple structure" (Richman 1986) through the use of a rotation technique such as the varimax rotation algorithm (Kaiser 1958). Barnston and Livezey (1987) is but one example of many studies that have used these methods successfully. However, application of such algorithms in the spectral domain results in EOFs that have simple structure in the spectral domain and regular structure in the physical domain. Indeed, the simplest pattern that could be achieved in the spectral domain would have a single non-zero spherical harmonic coefficient. But the corresponding spherical harmonic function has a regular, physical representation extending over the entire globe that does not fit our intuitive notion of simple local structure. When we actually applied Kaiser's (1958) varimax rotation to the spectral EOFs we did indeed recover patterns that closely resembled spherical harmonic functions.

5 Optimal weights and minimal errors

We now return to the calculation of the MSEs described in Section 2. Minimising $\varepsilon_{(lm)}$ subject to Eq. (4) we find that the optimal weights are

$$\vec{\mathbf{w}} = \mathscr{M}^{-}(\vec{\mathbf{b}} - \vec{\mathbf{1}}\Lambda), \tag{19}$$

where $\mathscr{M}^{-}$ is the generalised Moore-Penrose inverse of the $N \times N$ matrix

$$\mathscr{M}_{ij} = \rho(\vec{\mathbf{n}}_i, \vec{\mathbf{n}}_j)\Re[Y^{*}_{lm}(\vec{\mathbf{n}}_i)Y_{lm}(\vec{\mathbf{n}}_j)], \tag{20}$$

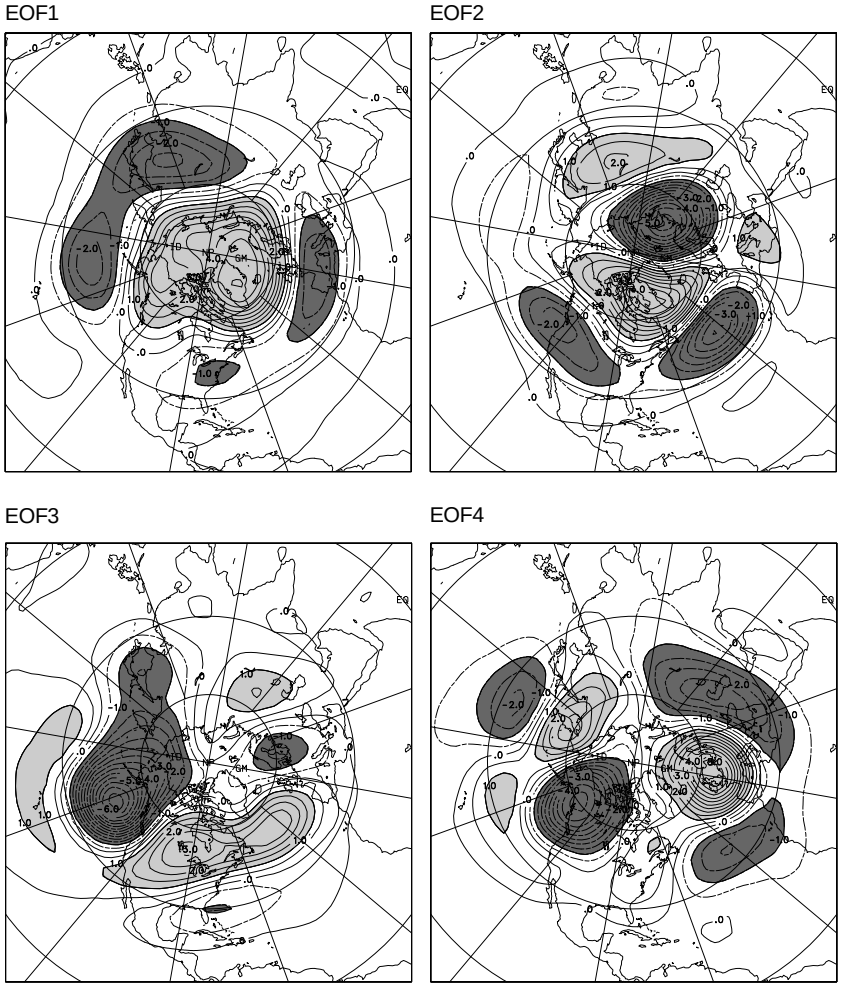

Fig. 5. EOFs 1–4 of CCC GCM2 monthly mean DJF Z_{500} explaining 13.8%, 9.4%, 8.9% and 6.5% of variance respectively. These patterns are essentially flat in the SH and tropical regions (not shown)

$\vec{\mathbf{b}}$ is the N dimensional vector

$$b_j = \sum_{k=1}^{(L+1)^2} \lambda_k \Re[\psi_{k,lm} Y^*_{lm}(\vec{\mathbf{n}}_j)] \psi_k(\vec{\mathbf{n}}_j), \tag{21}$$

$\vec{\mathbf{1}}$ is the N dimensional vector of units and Λ is the Lagrange multiplier

$$\Lambda = (\vec{\mathbf{1}}' \mathscr{M}^- \vec{\mathbf{b}} - 4\pi)/(\vec{\mathbf{1}}' \mathscr{M}^- \vec{\mathbf{1}}). \tag{22}$$

Equation (19) is evaluated by replacing covariance $\rho(\vec{\mathbf{n}}_i, \vec{\mathbf{n}}_j)$ in (20) with an estimate

$$\hat{\rho}_{ij} = \frac{1}{Q} \sum_{q=1}^{Q} S(\vec{\mathbf{n}}_i, t_q)\, S(\vec{\mathbf{n}}_j, t_q) \tag{23}$$

computed from a sample of Q realisations of the anomaly field S that were obtained at times t_q and observed at network locations $\vec{\mathbf{n}}_j$. This yields a unique set of weights w_j when $\mathscr{M}$ is of full rank. Otherwise Eq. (19) is one of infinitely many choices of weights that minimise Eq. (15). Standard theorems regarding the null spaces of linear operators (see, for example Strang 1980, p96) can be used to argue that $rank(\mathscr{M}) \leq rank(\hat{\rho})$ and that $rank(\hat{\rho}) \leq min(N, Q, (L+1)^2)$. In the examples we consider N varies from 24 to 210, $Q = 162$, 180, or 684 and $L = 21$.

When $Q - rank(\hat{\rho})$ is small or zero we should be concerned about the effects of artificial predictability (Davis 1976) on the estimated MSE. In these circumstances, the optimal weights estimated with Eq. (19) have the freedom to "adapt" to the data in the network with the result that the MSE may be under-estimated. We therefore use a cross-validation procedure to guard against the effects of artificial predictability. In each cross-validation step the data are divided into a "learning" data set and a verification data set. The learning data set is used to construct estimates of the model's EOFs and corresponding optimal weights. The MSE is estimated from the verification data set using Eq. (15) and the weights and EOFs derived from the learning data set. The process is repeated six times, each time excluding one entire simulation from the learning data set for use as the verification data set. The six MSE estimates obtained in this way are averaged to produce the cross-validated MSE estimate.

We consider five observing networks. Network 1R has 24 stations located on four latitude rings located at 50 °S, 15 °S, 15 °N and 50 °N. Each ring contains six equidistant stations. One station on each ring is positioned at 30 °E longitude. The "R" in the designation identifies the rectangular station configuration. Network 2 is a 24 station

Table 2. The MSE of the (0,0) spherical harmonic coefficient estimated with optimal weights expressed as a percentage of the variance of the true (0,0) coefficient. The cross-validated MSE is displayed in brackets

		T_s			Z_{500}		
Network	N	DJF	JJA	All	DJF	JJA	All
1R	24	67 (87)	31 (40)	73 (78)	100 (149)	56 (79)	88 (96)
1D	24	43 (60)	32 (40)	65 (70)	75 (104)	56 (86)	86 (95)
2	24	56 (84)	28 (38)	49 (53)	52 (79)	33 (45)	73 (78)
3	62	13 (40)	7 (18)	20 (24)	13 (35)	11 (27)	19 (24)
4R	64	10 (30)	5 (14)	15 (19)	3 (9)	2 (5)	4 (5)
4D	64	8 (20)	4 (11)	14 (17)	2 (6)	2 (6)	4 (5)
5R	240	0.02 (14)	0.008 (6)	1 (3)	0.001 (0.7)	0.00003 (0.5)	0.08 (0.2)
5D	240	32 (8)	0.0001 (2)	0.3 (0.8)	0.0004 (0.4)	0.0006 (0.2)	0.03 (0.08)

subset of the 63 station Angell-Korshover (1983; see also Trenberth and Olson 1991) network. Network 3 (62 stations) is the Angell-Korshover network with only the South Pole station excluded. Network 4R has 64 stations arrayed on eight latitude rings located at 70 °S, 50 °S, 30 °S, 10 °S, 10 °N, 30 °N, 50 °N and 70 °N. Each ring has eight equidistant stations with one station positioned at 23 °E longitude. Network 5R is a denser 210 point $24^\circ \times 12^\circ$ network in which first column of stations is located at 12 °E longitude and the first row at 78 °S latitude. We also consider variants of networks 1R, 4R and 5R in which every second row of stations is shifted zonally by half a grid length. We refer to the resulting diamond-shaped networks as networks 1D, 4D and 5D respectively.

The estimated MSEs of the spherical harmonic coefficient estimates, obtained from the full data set and via cross-validation, are compared with the coefficient variance

$$\sigma^2_{(lm)} = \langle |S_{lm}|^2 \rangle. \tag{24}$$

This variance can be expressed in terms of the spectrally transformed EOFs as

$$\sigma^2_{(lm)} = \sum_{k=1}^{(L+1)^2} \lambda_k |\psi_{k,lm}|^2. \tag{25}$$

We express the mean squared sampling error in dimensionless units as the ratio $\varepsilon^2_{(lm)}/\sigma^2_{(lm)}$. The improvement gained from using the optimal weights can be guaged by comparing this ratio with that obtained using uniform weights $w_j = 4\pi/N$.

Results for the (0,0) spherical harmonic coefficient (i.e, the global mean) are displayed in Table 2 (optimal weights) and Table 3 (uniform weights). We note:

a. The optimal weights (Table 2) very effectively reduce the estimated MSEs obtained with uniform weights (Table 3). Table 2 shows that the global mean 500 hPa height can be estimated with less than 10% mean squared error using a regular, optimally weighted, 64 station network. The error is approximately an order of magnitude greater when stations are uniformly weighted. The cross-validated MSE of the estimated global mean screen temperature is estimated to be 11% (14%) in JJA and 20% (30%) in DJF when a regular diamond-shaped (rectangular) 64 station network is optimally weighted. While the improvement with optimal weighting is not as great with T_s as with Z_{500}, the optimal weighting still results in cross-validated MSEs that are 3–7 times less than their uniformly weighted counterparts.

Table 3. The MSE of the (0,0) spherical harmonic coefficient estimated with uniform weights expressed as a percentage of the variance of the true (0,0) coefficient

		T_s			Z_{500}		
Network	N	DJF	JJA	All	DJF	JJA	All
1R	24	267	141	197	253	226	265
1D	24	277	138	221	246	213	235
2	24	259	118	208	243	126	180
3	62	138	50	101	132	80	110
4R	64	87	65	93	67	62	63
4D	64	89	83	109	67	60	64
5R	240	71	47	72	115	84	102
5D	240	67	44	66	106	84	102

b. Mean squared errors are somewhat less in JJA than in DJF for both T_s and Z_{500}. The effect is more pronounced for T_s than for Z_{500}. The explanation is that the variance of both variables is spatially more homogeneous in JJA. To illustrate the effect of eliminating variance inhomogeneity completely, we standardised T_s and Z_{500} so that the fields have unit variance everywhere at all times of the year. After doing this the cross-validated MSE estimates are reduced substantially beyond those shown in Table 2. For example, when using network 3 (62 quasi-regularly spaced points), the cross-validated MSE for the global mean is reduced in DJF to 20% for T_s and 9% for Z_{500}.

c. MSE estimates for T_s are greater than those for Z_{500}, even when the fields are standardised so that they have unit variance everywhere at all times of the year. The explanation is that Z_{500} has a "larger" spatial correlation structure (i.e., teleconnections operate over longer distances, especially in the tropics) than T_s. Hence Z_{500} has fewer spatial degrees of freedom than T_s and consequently the global mean of Z_{500} can be specified more accurately with the same number of points than can the global mean of T_s.

d. The network configuration affects the MSEs. When stations are laid out on a diamond-shaped grid, the cross-validated MSEs are smaller than for the corresponding rectangular networks (Table 2). Also, the 62 point network does not perform as well as either 64 point network (at least for the global mean). The diamond-shaped networks

do better than the corresponding rectangular networks because their stations have greater mean separation distance and hence sample more non-redundant (i.e., correlated) information than the rectangular networks.

e. The real (i.e., cross-validated) MSEs are, with one exception, greater than the MSE estimates obtained from the full data set. This is partly accounted for by the fact that the learning data set used in the cross-validation procedure is only (5/6) th the size of the full data set. Hence there is additional sampling uncertainty in the covariance structure estimates that are used during cross-validation. However, adaptation of the weights to the data (i.e., the artificial skill phenomenon) is also a factor. In the small networks, where the data are used to determine only a small number of weights, there is less opportunity for adaptation than in the larger networks. One speculates that the increased MSE estimates obtained with cross-validation for small networks are due primarily to the increased uncertainty in the covariance structure estimates that are used. Note that this source of uncertainty is greatest in DJF ($Q = 162$) and least when all months are used ($Q = 684$). The effects of the increasing opportunity for adaptation of the weights to the data can be seen as the networks grow. As the networks become large, the relative discrepancy between the cross-validated MSE and unvalidated MSE estimates increases. The combination of small sample and large network (when the rank of matrix $\mathscr{M}$ in Eq. (19) is less than the number of points in the network) leads to the greatest uncertainty in the unvalidated MSE estimates. Thus, while the cross-validated MSE estimates are somewhat inflated because not all data are used to estimate the covariance structure, they are the only reliable guide to the accuracy with which a spherical harmonic coefficient can be estimated from a given network when the sample size is small relative to network size.

The cross-validated DJF MSEs are displayed for all spherical harmonic coefficients in Figs. 6 (T_s) and 7 (Z_{500}). The diagrams display the MSEs as a function of the Legendre polynomial index l on the vertical axis and the Fourier index m on the horizontal axis. We show only the MSEs for $m \geq 0$ because they are symmetric about $m = 0$. To make the diagrams easier to read we display $100 \times Log_{10}(\hat{\varepsilon}^2_{(lm)}/\hat{\sigma}^2_{(lm)})$ so that the zero contour indicates MSEs equal to 100% of the corresponding coefficient variance. Coefficients in regions outside the zero contour cannot be estimated from the network considered. The contour interval is chosen so that each contour increment represents a doubling of the MSE. The spectral region in which the MSE is less than 50% of the coefficient variance has light shading, and the region in which the MSE is less than 10% of the coefficient variance has dark shading.

The conclusions that can be drawn from these diagrams are in many respects similar to those derived from Tables 2 and 3. We note that:

a. The size of the spectral region in which coefficients can be reliably estimated increases with network density.

b. Comparing T_s (Fig. 6) with Z_{500} (Fig. 7), we see that the spectral coefficients of Z_{500} are more easily estimated from a given network than those of T_s. This happens because Z_{500} has larger correlation structures than T_s.

c. For T_s, the regular networks (Fig. 6a, c) perform similarly to the irregular networks (Fig. 6b, d) of comparable size.

d. For Z_{500}, the 24 point irregular network (Fig. 7b) provides slightly better estimates of the low order real (i.e., $m = 0$) spherical harmonic coefficients than the regular 24 point network (Fig. 7a). In contrast, the regular 64 point network (Fig. 7c) performs better than the 62-point irregular network (Fig. 7d). The regular network is able to estimate a number of coefficients with cross-validated MSEs of less than 10% while the irregular network is not able to do this.

e. The regular networks are more strongly affected by aliasing error than the irregular networks. For example, compare the upper left hand corners of Fig. 7a and 7c with those of Fig. 7b and 7d.

f. The effect of network configuration (whether rectangular or diamond-shaped) can be seen by comparing panels e and f of Figs. 6 and 7. For T_s (compare Fig. 6e, f) the low-order spherical harmonic coefficients can be estimated with greater precision with the diamond-shaped network. For Z_{500} (compare Fig. 7e, f) the estimates of the high Fourier index coefficients improve, particularly for the Legendre polynomials of order $l = 6$ to $l = 10$. In both cases these improvements occur because the diamond-shaped network extracts more non-redundant information from the climate field than the rectangular network.

g. Optimal weighting expands the domain in which useful coefficient estimates can be made and very substantially improves the accuracy that can be obtained at the largest scales. This can be seen by comparing Fig. 8, which shows the MSEs of DJF spherical harmonic coefficient estimates made by uniformly weighting the rectangular 210 point network, with Fig. 7e, f. Note in Fig. 8b that useful coefficient estimates cannot be made for Z_{500} beyond zonal wave number $m = 7$. This is all that can be expected from a rectangular network that has 15 points in the zonal direction. The diamond-shaped network (not shown) is able to slightly exceed this bound because of the staggering of grid points on adjacent latitude circles. Because Z_{500} de-correlates relatively slowly in the meridional direction, the staggered grid points in adjacent rows provide information about the behaviour of Z_{500} on a zonal scale that is somewhat smaller than the zonal grid spacing. A hint of this phenomenon can be seen by comparing the zonal wave number $m = 6, \ldots, 10$ regions in Fig. 7e and f.

h. In JJA the performance of the regular 64- and 210-point networks improves while that of the irregular 62-point network degrades slightly. Apparently the regular networks are able to take advantage of the greater homogeneity in JJA. Figure 9 displays the cross-validated MSEs in JJA for the optimally weighted 210 point rectangular network. Comparing with Figs. 6e and 7e, we see that the domain in which useful spherical harmonic coefficients can be made expands in JJA for both T_s and Z_{500}. Also note that the zonal wave number $m = 7$ resolution boundary can be clearly seen in Fig. 9b.

i. The "optimal" weights we compute for the larger networks for DJF and JJA are far from being truly optimal. The reason for this is the substantial uncertainty in

the spatial covariance structure estimates computed from the modest amount of GCM output available ($Q = 162$ in DJF and $Q = 180$ in JJA) at the scales resolved by the larger networks considered. Some impression of the effect of error in the estimated covariance structure can be obtained from Fig. 10 where we display the cross-validated MSEs for the optimally weighted 210 point rectangular network when all $Q = 684$ months of data are

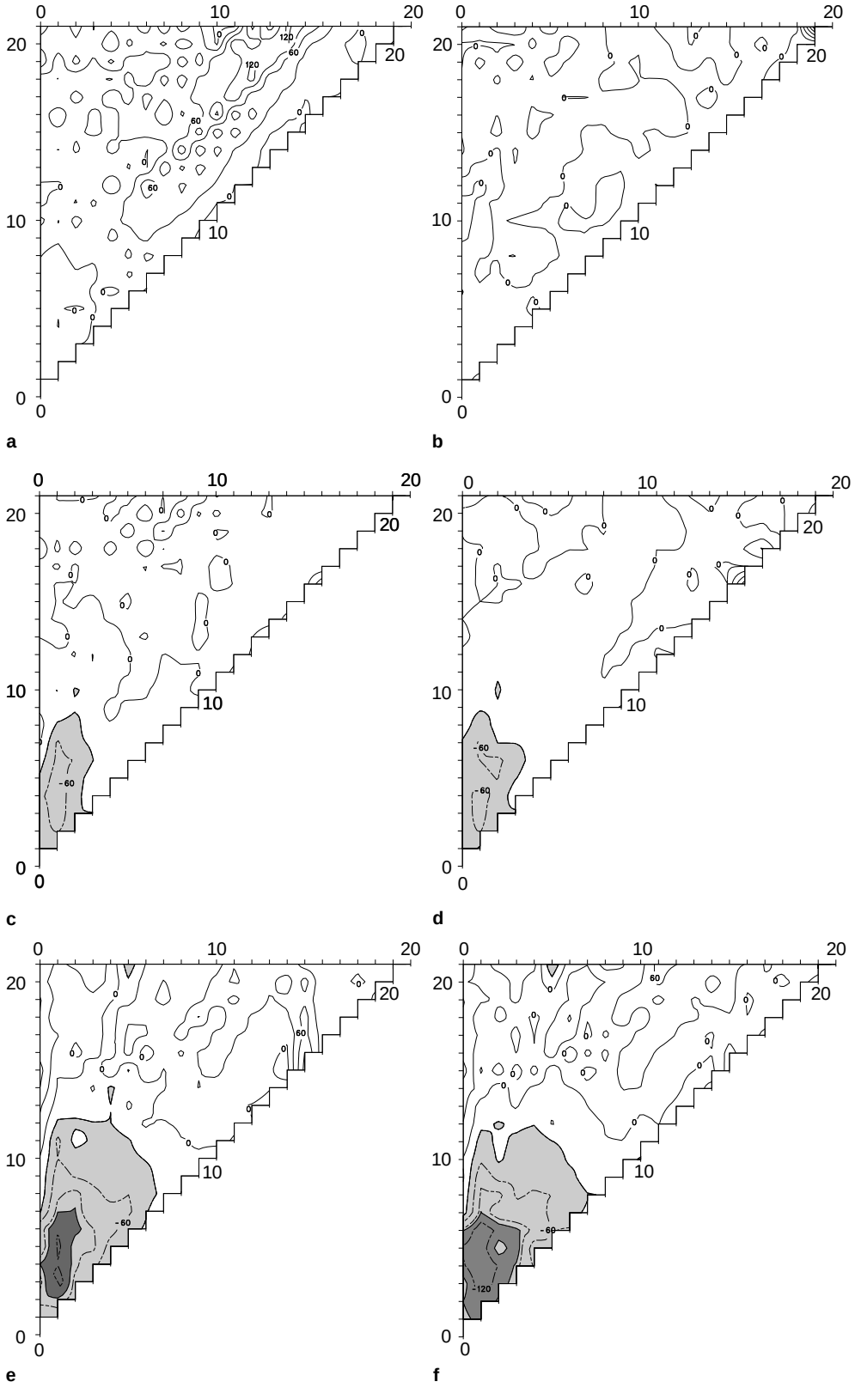

Fig. 6a–f. Cross-validated MSE for DJF T_s (see text) for **a** 24 point rectangular network, **b** 24 point subset of the A–K network, **c** 64-point rectangular network, **d** 62 point A–K network, **e** 210 point rectangular network and **f** 210 point diamond-shaped network

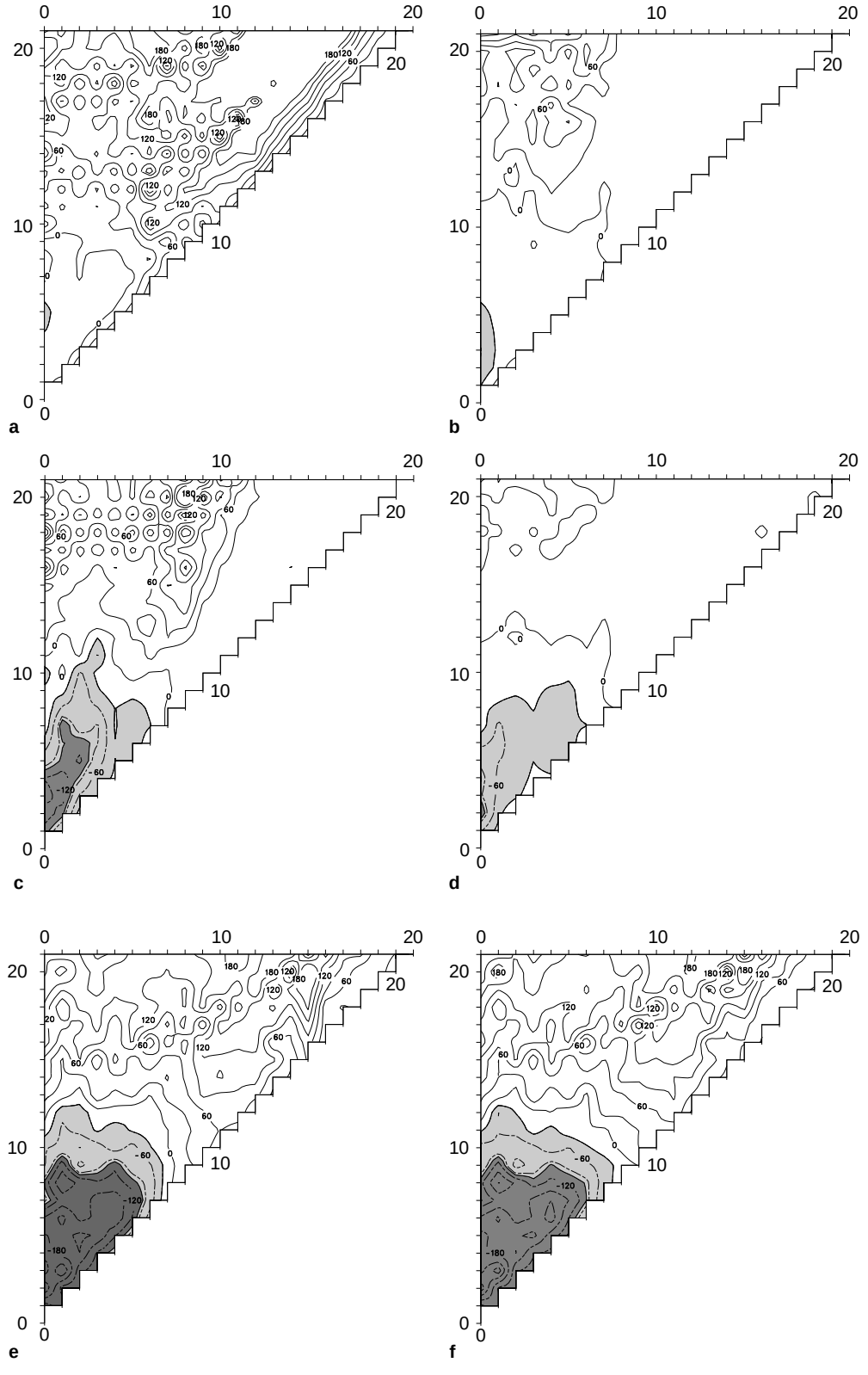

Fig. 7a–f. As Fig. 6, except that the cross-validated MSE for DJF Z_{500} is displayed

used. Comparing Fig. 10 with Figs. 6e, f, 7e, f and 9, we see that imperfectly estimated EOFs have a large impact on the precision of spherical harmonic coefficient estimates at all scales. As an aside, note that the $m = 7$ resolution boundary is now seen clearly for both T_s and Z_{500}. For T_s this boundary becomes parallel to the l axis only asymptotically, indicating that T_s becomes isotropic much more slowly than Z_{500}.

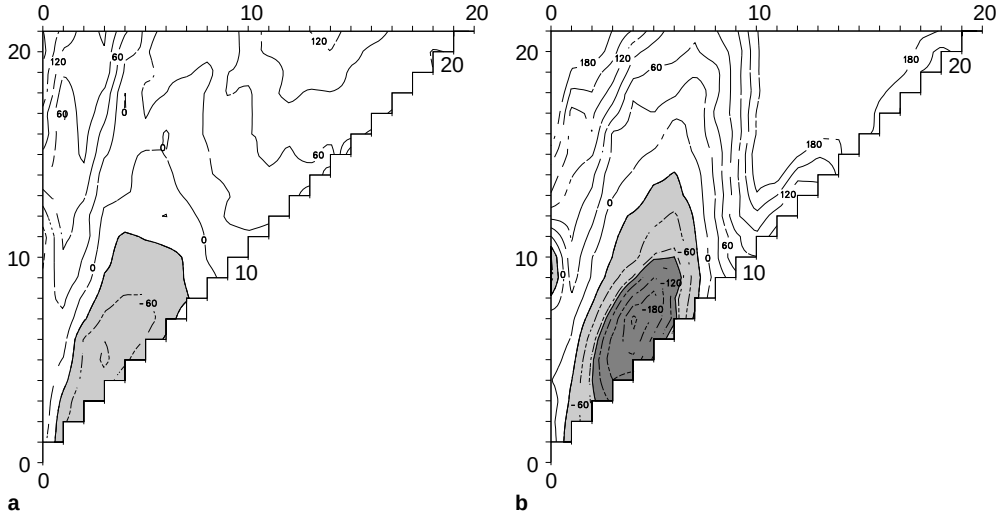

Fig. 8a,b. MSE of spherical harmonic coefficients estimated from the uniformly weighted 210 point rectangular network. The MSE is displayed as $100 \times Log_{10}(\hat{\varepsilon}^2_{lm}/\hat{\sigma}^2_{lm})$. **a** DJF T_s **b** DJF Z_{500}

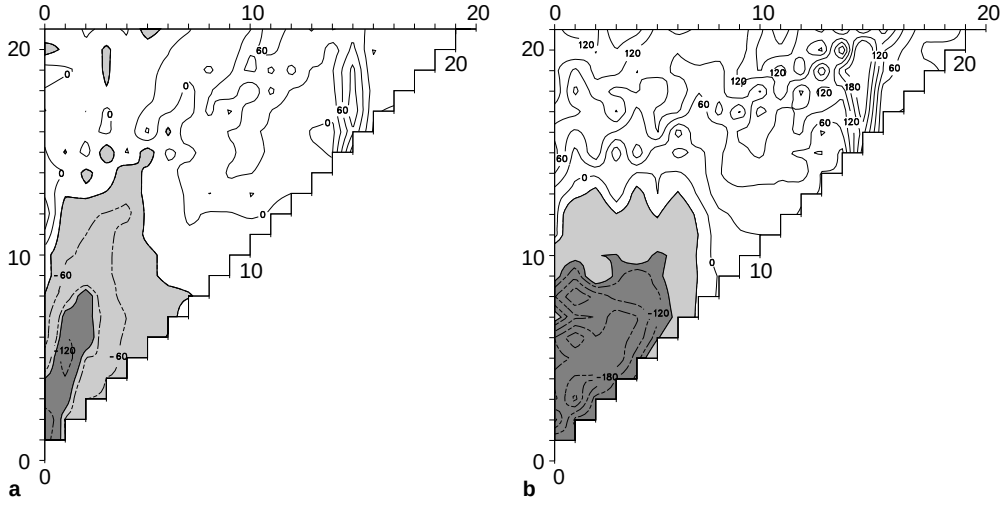

Fig. 9a,b. MSE of spherical harmonic coefficients estimated from the optimally weighted 210 point rectangular network. The MSE is displayed as $100 \times Log_{10}(\hat{\varepsilon}^2_{lm}/\hat{\sigma}^2_{lm})$. **a** JJA T_s, and **b** JJA Z_{500}

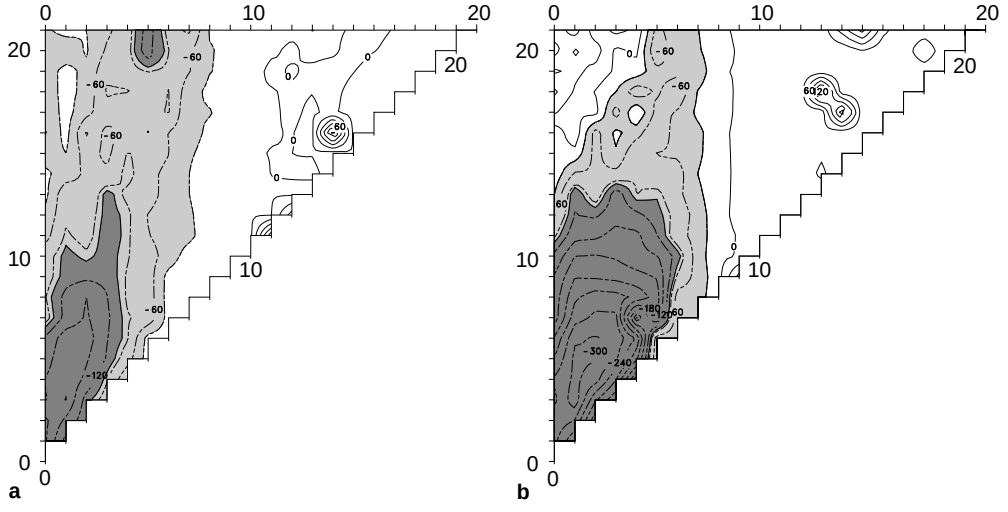

Fig. 10a,b. As Fig. 9, except for all months of the year

6 Summary and conclusions

In this study we have reviewed a methodology for optimally estimating spherical harmonic coefficients from observations taken at a small number of observing points. The estimates are made by weighting the observations so as to minimise the mean squared error. The method can be generalised so that it applies to any pattern coefficient, including the greenhouse gas fingerprints that are used in climate change detection studies.

In Sect. 2 we analysed the structure of the errors incurred when using a small observing network to estimate the time dependent spherical harmonic coefficients of a field S. The estimates are constructed (Eq. 3) as a weighted linear combination of field values at the network locations. First, for convenience and mathematical clarity, the spatial covariance structure of S is decomposed into EOFs. Each EOF is then given its own spherical harmonic function expansion (Eq. 14). Next, the EOFs are evaluated at the network locations and Eq. (3) is used to approximate the EOF's spherical harmonic coefficients. Finally, Eq. (15) shows that the MSE of the estimated (l, m) spherical harmonic coefficient of field S is a linear combination of the errors incurred when using Eq. (3) to approximate the corresponding spherical harmonic coefficient of the EOFs. The approximation error for each EOF is weighted by the corresponding eigen-value.

In Sect. 5 we showed how to weight the network locations to minimise the MSE of the estimator of a given spherical harmonic coefficient. The weights, which are different for every spherical harmonic, see Eqs. (20), (21) and (19), are determined by the station locations and the spatial covariance structure of the field.

We applied the methodology to an ensemble of six 10-y AMIP simulations performed with the Canadian Climate Centre 2nd generation general circulation model (CCC GCM2). We estimated the covariance structure of the simulated monthly mean T_s and Z_{500} fields and used it to determine optimal weights for a number of small networks. The MSE of estimation was subsequently calculated for each spherical harmonic coefficient and network configuration. A cross-validation procedure was used to protect against the artificial skill that accrues from using the same data set to determine the weights and estimate the MSEs.

CCC GCM2 was described briefly in Sect. 3 as were the variance and correlation structures of the model's monthly mean T_s and Z_{500} in DJF and JJA. We saw that both the variance and correlation structures are highly inhomogeneous, and that these structures change with the annual cycle.

The EOFs of the simulated monthly mean fields were computed in the spectral domain (Sect. 4) because, in this study, the eigen-analysis problem has a convenient and compact spectral representation. The EOFs of the model's monthly mean Z_{500} fields were seen to compare well with patterns obtained from observations. The T_s EOFs are likely less reliable because they have been heavily influenced by observed SST and sea–ice extent during the AMIP decade (1979–88).

We analysed the performance of eight small networks in three configurations. Specifically, we considered 24, 64 and 210 point regular networks in rectangular and diamond-shaped latitude–longitude arrangements and also considered 24 and 62 point versions of the Angell-Korshover (1983) network.

We found that it was very important to cross-validate MSE estimates, particularly when the sample available for estimating EOFs is small relative to the number of points in the network. Without cross-validation the expected MSE is underestimated because uncertainty in the estimates of the optimal weights is not taken into account.

Despite our caution, we found the optimal weighting to be very effective at reducing the expected MSE in comparison with uniform weighting. The number of coefficients that can be estimated with a given precision was seen to depend upon the covariance structure, the network density and the network configuration.

We saw that cross-validated MSEs were smaller in JJA than in DJF and we attributed that to reduced variance inhomogeneity in JJA. We illustrated the effect of variance inhomogeneity on MSEs by standardising T_s and Z_{500} to eliminate variance inhomogeneity.

We argued that spatial correlation structure also affects MSEs. Given a particular network, spherical harmonic coefficients of fields with larger spatial correlation structure have smaller MSEs for the scales that are resolvable by the network.

Finally, we saw that the network configuration has an effect. The diamond-shaped network improves on the rectangular network by sampling more non-redundant information. The rectangular networks generally did better than the irregular networks on the scales that they resolved. But, the irregular networks were less affected by aliasing error than their regular counterparts.

Several lines of investigation remain open for us at this point. First, our results for T_s are likely to be strongly influenced by the SST and sea–ice extents observed during the AMIP decade. Thus, our calculations will be repeated with a coupled atmosphere-ocean version of CCC GCM2. Also, longer simulations are needed to reduce EOF uncertainty and artificial skill. Second, larger, but much more heterogeneous networks that more closely reflect the current operational observing networks should be examined. Third, aliasing error that results from the interaction between the network configuration and a field's spatial covariance structure is but one source of uncertainty in coefficient estimates. Random observational error is another source that should be accounted for. Finally, the methods we have described in this work should be revisited to make them robust to outliers that result, for example, from data transcription error.

Acknowledgements. The authors wish to thank the Climate Variability Node of the Canadian Institute for Climate Studies for financial support and acknowledge that work by Dr. Shen was also supported by an Atmospheric Environment Service, Canada, science subvention. We are very grateful for useful and constructive comments that were provided by John Fyfe and Mark Holzer.

References

Angell JK, Korshover J (1983) Global temperature variations in the troposphere and stratosphere, 1958–1982. Mon Weather Rev 111:901–921

Barnett TP, Schlesinger ME (1987) Detecting changes in global climate induced by greenhouse gases. J Geophys Res 92 : 14772–14780

Barnett TP, Schlesinger ME, Jiang X (1991) On greenhouse gas signal detection strategies. In: Schlesinger ME (ed) Greenhouse-gas-induced climatic change: a critical appraisal of simulations and observations. Elsevier, Amsterdam, pp 537–558

Barnston AG, Livezey, RE (1987) Classification, seasonality, and persistence of low-frequency atmospheric circulation patterns. Mon Weather Rev 115 : 1083–1126

Boer GJ, McFarlane NA, Lazare M (1992) Greenhouse gas-induced climate change simulated with the CCC second-generation general circulation model. J Clim 5 : 1045–1077

Daley R (1991) Atmospheric data analysis. Cambridge University Press, Cambridge, UK, 457pp

Davis RE (1976) Predictability of sea surface temperature and sea level pressure anomalies over the North Pacific Ocean. J Phys Ocean 6 : 249–266

Gandin LS (1963) Objective analysis of meteorological fields. Gridrometeoizdat, Lenningrad, 287pp

Gates WL (1992) The Atmospheric Model Intercomparison Project. Bull Am Meteorol Soc 73 : 1962–1970

Hasselmann K (1993) Optimal fingerprints for the detection of time dependent climate change. J Clim 6 : 1957–1971

Jones PD, Raper SCB, Bradley RS, Diaz HF, Kelly PM, Wigley TML (1986a) Northern Hemisphere surface air temperature variations, 1851–1984. J Clim Appl Meteorol 25 : 161–179

Jones PD, Raper SCB, Bradley RS, Diaz HF, Kelly PM, Wigley TML (1986b) Southern Hemisphere surface air temperature variations, 1851–1984. J Clim Appl Meteorol 25 : 1213–1230

Kaiser HF (1958) The varimax criterion for analytic rotation in factor analysis. Psychometrika 23 : 187–200

Kim K-Y, North GR (1993) EOF analysis of surface temperature field in a stochastic climate model. J Clim 6 : 1681–1690

Kim K-Y, North GR, Shen SS (1996) Optimal estimation of spherical harmonic components from a sample with spatially nonuniform covariance statistics. J Clim 9 : 635–645.

McFarlane NA, Boer GJ, Blanchet J-P, Lazare M (1992) The Canadian Climate Centre second generation general circulation model and its equilibrium climate. J Clim 5 : 1013–1044

North GR, Kim K-Y, Shen SS, Hardin JW (1995) Detection of forced climate signals. Part I: filter theory. J Clim 8 : 409–417

Oort AH (1983) Global atmospheric circulation statistics, 1958–1973. NOAA Prof Pap 14, US Department of Commerce, Rockville, Md, 180pp

Reynolds RW, Smith TM (1994) Improved global surface temperature analyses using optimum interpolation. J Clim 7 : 929–948

Richman MB (1986) Rotation of principal components. J Climatol 6 : 293–335

Shea DJ (1986) Climatological Atlas: 1950–1979. Surface air temperature, precipitation, sea-level pressure, and sea-surface temperature (45 °S–90 °N). NCAR/TN-269 + STR. NCAR, Boulder, CO, 194pp + 10fiche

Shen SS, North GR, Kim K-Y (1994) Spectral approach to optimal estimation of the global average temperature. J Clim 7 : 1999–2007

Shen SS, North GR, Kim K-Y (1996) Optimal estimation of the spherical harmonic components of the surface air temperature. Environmentrics 7 : 261–276

Smith TM, Reynolds RW, Ropelewski CF (1994) Optimal averaging of seasonal sea surface temperatures and associated confidence interval (1860–1989). J Clim 7 : 949–964

Strang G (1980) Linear algebra and its applications, 2nd Edn. Academic Press, 414pp

Thiebaux HJ (1976) Anisotropic correlation functions for objective analysis. Mon Weather Rev 104 : 994–1002

Thiebaux HJ, Pedder MA (1987) Spatial objective analysis: with applications in atmospheric science. Academic Press, 299 pp

Trenberth KE, Olson JG (1991) Representativeness of a 63-station network for depicting climate changes. In: Schlesinger ME (ed) Greenhouse-gas-induced climatic change: a critical appraisal of simulations and observations. Elsevier, Amsterdam pp 249–259

Vinnikov KY, Groisman PY, Lugina KM (1990) Empirical data on contemporary global climate changes (temperature and precipitation). J Clim 3 : 662–677

Wallace JM, Gutzler DS (1981) Teleconnections in the geopotential height field during the Northern Hemisphere winter. Mon Weather Rev 109 : 784–812

Zwiers FZ (1996) Interannual variability and predictability in an ensemble of AMIP climate simulations conducted with the CCC GCM2. Clim Dyn 12 : 825–847